China Instrument and Control Society
Instrumentation
INSTRUMENTATION, Vol. 11, No. 2, June 2024 https://doi.org/10.15878/j.instr.202400059

Article

Multi-Modal Medical Image Fusion Based on Improved Parameter Adaptive PCNN and Latent Low-Rank Representation

Zirui Tang, Xianchun Zhou*

School of Artificial Intelligence (School of Future Technology), Nanjing University of Information Science &Technology, Nanjing 210000, China

* Corresponding author email: zhouxc2008@163.com

Abstract: Multimodal medical image fusion can help physicians provide more accurate treatment plans for patients, as unimodal images provide limited valid information. To address the insufficient ability of traditional medical image fusion solutions to protect image details and significant information, a new multimodality medical image fusion method (NSST-PAPCNN-LatLRR) is proposed in this paper. Firstly, the high and low-frequency sub-band coefficients are obtained by decomposing the source image using NSST. Then, the latent low-rank representation algorithm is used to process the low-frequency sub-band coefficients; An improved PAPCNN algorithm is also proposed for the fusion of high-frequency sub-band coefficients. The improved PAPCNN model was based on the automatic setting of the parameters, and the optimal method was configured for the time decay factor αe. The experimental results show that, in comparison with the five mainstream fusion algorithms, the new algorithm has significantly improved the visual effect over the comparison algorithm, enhanced the ability to characterize important information in images, and further improved the ability to protect the detailed information; the new algorithm has achieved at least four firsts in six objective indexes.

Keywords: image fusion; improved parameter adaptive pcnn; non-subsampled shear-wave transform; latent low-rank representation

Citation: Tang, Zirui, and Xianchun Zhou. "Multi-Modal Medical Image Fusion Based on Improved Parameter Adaptive PCNN and Latent Low-Rank Representation." Instrumentation 11, no. 2 (2024). https://doi.org/10.15878/j.instr.202400059.

1 Introduction

Medical images are acquired in a myriad of ways. Medical images of different modalities convey different visual information, but it is difficult for a single modality to convey the full information of tissues (MR) or organs (CT). The ultimate goal of medical image fusion technology[1,2] is to integrate the useful information from multiple images into one image, which can help doctors analyze medical images in depth, improve the accuracy of diagnosis and provide more appropriate treatment plans for patients.

Since the middle of the last century, various medical image fusion algorithms[3-6] have been widely used. Among them, the multi-scale transform (MST) based image fusion scheme has become the preferred research direction for many scholars because of its excellent fusion performance and good visual perception effect. The NSST algorithm proposed in the literature[7] is the result of improvement based on retaining the advantages of shear wave transform, which avoids the generation of pseudo-Gibbs phenomenon, operates with high efficiency and low complexity, and details such as edges and contours in the source image can be extracted effectively; Johnson has developed a pulse-coupled neural network (PCNN) model[8-10] to reduce computational complexity while preserving basic visual cortical properties, but the problem of precise parameter setting in the model seriously restricted the further development of PCNN; Literature[11] proposed that in the framework of NSST(Non-Subsampled Shearwave Transform), PCNN was added into fusion rules to effectively extract image

gradient features and retain information, but many parameters within PCNN were set with low accuracy; literature[15] proposed a simplified SPCNN model-based image segmentation method, automatic setting of parameters by the SPCNN model to achieve better segmentation; The literature[16] improved the SPCNN model to obtain a parametric adaptive PAPCNN model. The experiments showed that the convergence speed of PAPCNN model was significantly improved and the application in image fusion also gave better experimental results.

Literature[12] proposed a low-rank representation (LRR) image fusion algorithm, which captured the global structure of the source image, but had limited local structure retention capability due to the lack of dictionary learning in LRR; literature[13] used the K-SVD algorithm to learn various types of sub-dictionaries and then constructed a global dictionary, which achieved good fusion results in both global and local structures; The literature[14] used a weighted averaging strategy and a summation strategy to fuse global and local structure information, improved clarity of fused image detail information respectively.

In view of the problems of current mainstream image fusion algorithms. In this paper, based on the PAPCNN model, an improved fusion algorithm—the NSST-PAPCNN-LatLRR algorithm, is proposed. The innovation points include the following two main points:

(1) The PAPCNN model is introduced into the multi-scale transform high-frequency partial fusion, which overcomes the problem of low accuracy of free parameter setting in the traditional PCNN model. In addition, the temporal decay factor is improved in the model to adjust the decay rate of the dynamic threshold, which significantly enhances the detail protection of the image.

(2) In this paper, the latent low-rank representation model is introduced into the multi-scale transformed low-frequency part of the fusion for the first time, which also contains some significant and detailed information in the low-frequency part. The LatLRR model overcomes the problem of significant information loss in the low-frequency portion of traditional multi-scale transform image fusion.

2 Related work

2.1 NSST

Fig.1 shows the decomposition process of NSST in detail. As a multiscale geometric analysis tool widely used in image processing, the NSST transform has the advantages of multi-directionality, translation invariance and low computational complexity. The multiscale decomposition process is implemented using a non-down sampling pyramidal filter combination filter (NSPF), which reduces the pseudo-Gibbs phenomenon and also overcomes the disadvantage of traditional multiscale transformation tools that do not possess translation invariance. SFB achieves directional localization. It is suitable for image processing with features such as translation invariance, sensitivity to edge contour feature information[17], and effective extraction of texture information from images[18]. Based on the above features, we choose NSST to complete the image decomposition and reconstruction process.

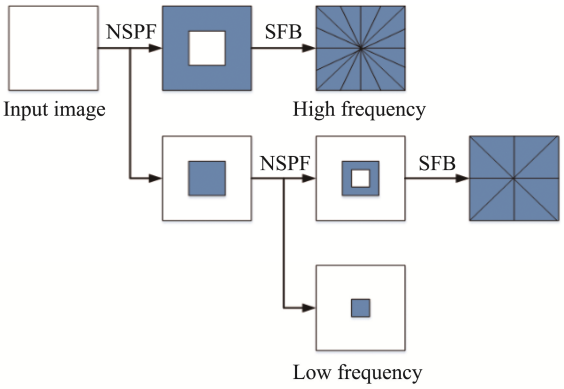

Fig.1 NSST decomposition schematic

2.2 Adaptive PCNN (PAPCNN)

The critical problem with applying the basic PCNN model to image fusion is the determination of the parameters. Such as temporal decay factor, connection

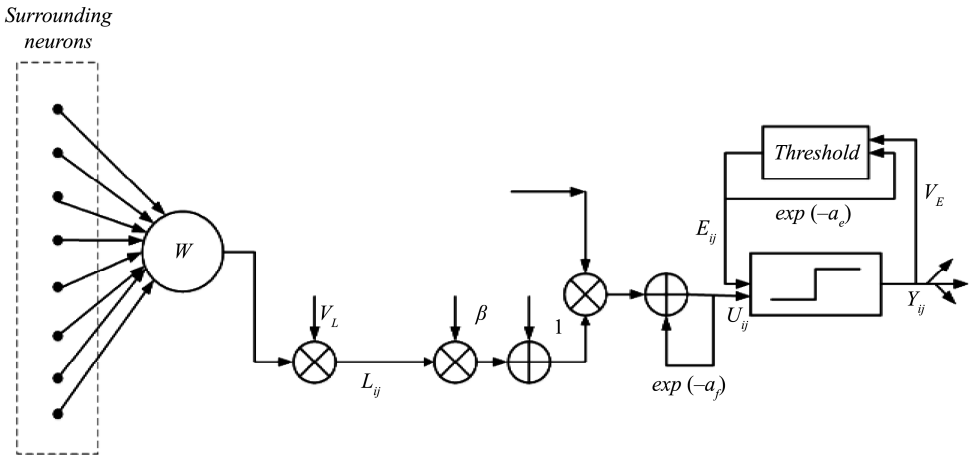

Fig.2 PAPCNN model architecture.

strength, and amplitude, etc. In order to avoid the manual selection of parameters that can easily cause significant experimental errors, Chen et al. [19] proposed a simplified SPCNN model based on PCNN, which simplified the problem of difficult parameter setting and low accuracy. A large amount of experimental data shows that the PAPCNN model also achieves good experimental results in image fusion, the overall image fusion quality is greatly improved.

$$\boldsymbol{F}_{ij}[n] = S_{ij} \tag{1}$$

$$L_{ij}[n] = V_L \sum_{kl} W_{ijkl} Y_{kl}[n-1] \tag{2}$$

$$U_{ij}[n] = e^{-\alpha_f} U_{ij}[n-1] + F_{ij}[n](1+\beta L_{ij}[n]) \tag{3}$$

$$Y_{ij}[n] = \begin{cases} 1, \ if \ \ \mathrm{U_{ij}}[n] > E_{ij}[n-1] \\ 0, \text{ otherwise} \end{cases} \tag{4}$$

$$E_{ij}[n] = e^{-\alpha_e} E_{ij}[n-1] + V_E Y_{ij}[n] \tag{5}$$

In the PAPCNN model, $F_{ij}[n]$ and V_L represent the input and connected input, respectively, for n iterations at the position (i, j). During the iterations, S_{ij} is the external input, fixedly attached to $F_{ij}[n]$. The previous firing state of $L_{ij}[n]$ and the adjacent neuron determines the present strength through synaptic weights. The PAPCNN model is shown in Fig.2.

The internal activity $U_{ij}[n]$ consists of its previous iteration value $e^{-\alpha f}U_{ij}[n–1]$ and the input together with the non-linear modulation $F_{ij}[n](1+\beta L_{ij}[n])$ connecting the inputs, where parameter α_f is the time decay factor of the internal activity $U_{ij}[n]$, and parameter β is the connection strength. The output $Y_{ij}[n]$ of the PCNN model determines the triggering event of the model and it has two states of output: $Y_{ij}[n]=1$ and $Y_{ij}[n]=0$. As shown in (4), When $U_{ij}[n]>E_{ij}[n–1]$, $Y_{ij}[n]=1$ and in fired. Updating the dynamic threshold $E_{ij}[n]$ by substituting the value of output $Y_{ij}[n]$ into (5), the parameter α_e is the time decay factor, V_E is the amplitude of $Y_{ij}[n]$. In the PAPCNN, the initial values of $Y_{ij}[0]$, $U_{ij}[0]$ and $E_{ij}[0]$ are all zero. Therefore, all non-zero strength neurons are excited in the first iteration. The architecture of the PAPCNN model is shown in Fig.2.

Equations (1) to (5) indicate that five parameters need to be set in the PAPCNN model: the amplitude V_E of the dynamic threshold E, the amplitude V_L of the connection input L, Time decay factor α_f for internal activity U and time decay factor α_e for dynamic threshold E, and the connection strength β. Furthermore, by the simplified (3) of the PAPCNN model, both β and V_L act as weighting factors for $\sum_{kl} W_{ijkl} Y_{kl}[n-1]$. Therefore, these two parameters can be treated as a whole λ. Thus only four parameters actually exist: α_e、α_f、$\alpha_f$and V_E.

2.3 Latent low-rank representation

The traditional LRR algorithm only considers the global structure of the image and the limited application range. Liu et al.[20] proposed the LatLRR algorithm based on the LRR theory, which can extract global and local structures from the source image and further enhance the protection of the main and local significant information. The algorithm can be simplified as follows (6):

$$\begin{aligned} &\min_{Z,L,E} \|Z\|_* + \|L\|_* + \lambda \|E\|_1 \\ &s.t., X = XZ + LX + E \end{aligned} \tag{6}$$

λ is the equilibrium coefficient and is constantly greater than zero, $\|\cdot\|_*$ is the kernel parametrization, and $\|\cdot\|_1$ is the L1 parametrization. Z is the low-rank coefficient matrix, L is the significant coefficient matrix, X is the observed data matrix, and E is the sparse noise component. XZ denotes the low-rank part of the image and LZ denotes the significant part of the image. The inexact augmented Lagrange multiplier (ALM) solves for the values of the components in (6).

LatLRR algorithm decomposed the image into low-rank part X_{lrr} and significant part X_S. The low-rank part contains more global structure information in the source image, and in order to better protect the contour information in the image, the weighted average strategy is used to process the low-rank part. The salient part mainly contains the salient features of the decomposed image, and the salient features of the source image need to be preserved in the fused image as much as possible, so the summation strategy is used to process the salient part.

3 NSST-PAPCNN-LatLRR fusion algorithm

The specific fusion steps of this algorithm are shown in Fig.3. First, decompose the image into high-frequency and low-frequency parts; then, the improved PAPCNN algorithm is used for the high-frequency part, and the latent low-rank algorithm is introduced into the low-frequency information fusion for the first time for the low-frequency part; finally, NSST reconstruction is performed to complete the image fusion process.

3.1 NSST decomposition

Firstly, the pre-aligned source images A and B are decomposed using NSST to obtain the decomposed sub-band coefficients $\left\{H_A^{l,k}, L_A\right\}$ and $\left\{H_B^{l,k}, L_B\right\}$. $H_A^{l,k}$ denotes the high-frequency sub-band coefficients of the source image A in the decomposition series L and decomposition direction k, L_A denotes the low-frequency coefficients of source image A after decomposition. Similar to A, $H_B^{l,k}$ and L_B denote the corresponding sub-band coefficients after the decomposition of image B.

3.2 High-frequency sub-band coefficient fusion

In this paper, the improved parametric adaptive PCNN (PAPCNN) model of Section 2 is used for the fusion of high-frequency sub-bands. In the fusion process of the high-frequency part, in order to better handle the fusion of high-frequency information, we use the absolute

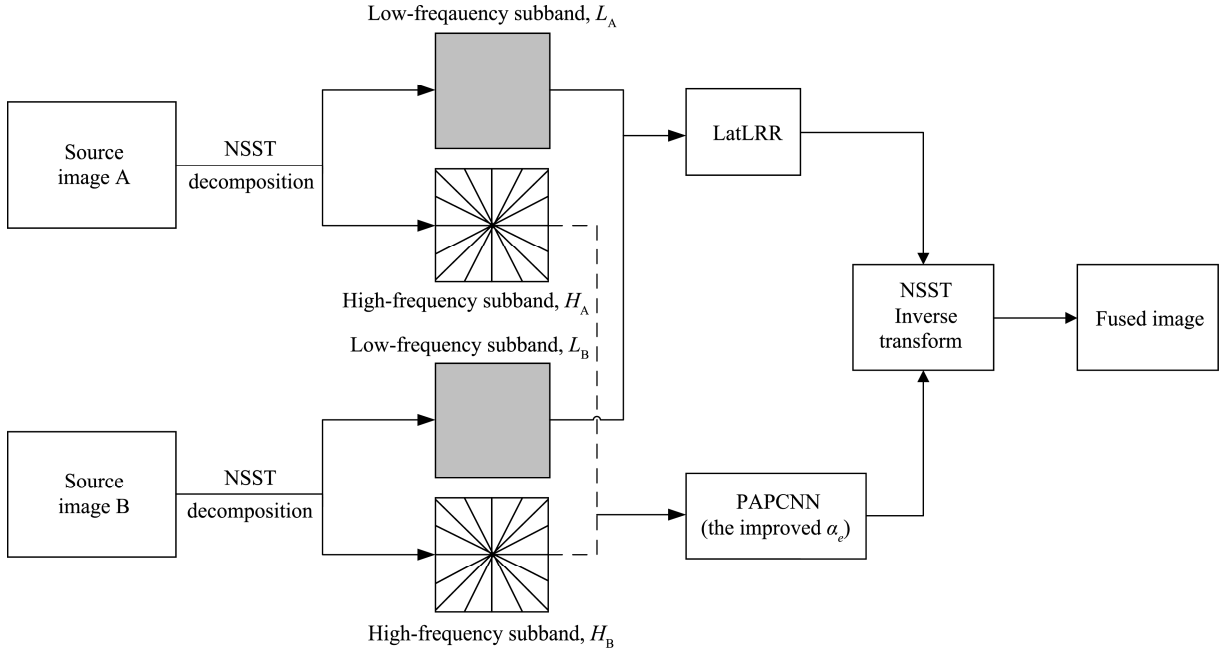

Fig.3 Flow chart of NSST-PAPCNN- LatLRR algorithm

value of the high-frequency coefficients in selecting the appropriate network input (Namely, the feed input is $F_{ij}[n]=\left|H_S^{l,k}\right| S\in\{A,B\}$), to achieve better fusion effect. During the iterations of the high-frequency part, the final launch time reflects the overall activity level of the high-frequency part to a certain extent. According to the basic formula of PAPCNN, the cumulative trigger time can be calculated from the sum of the last trigger time and the final output. As in (7):

$$T_{ij}[n]=T_{ij}[n-1]+Y_{ij}[n] \tag{7}$$

where N is the total number of iterations for the cumulative trigger time, $T_{ij}[n]$ is the trigger time of the neuron. $T_{A,ij}^{l,k}$ denotes the ignition time of the high-frequency sub-band $H_A^{l,k}$ in the PAPCNN model. has the same meaning for $H_B^{l,k}$. From (8) the fusion band is calculated:

$$H_F^{l,k}(i,j)=\begin{cases}H_A^{l,k}(i,j), & if\ T_{A,ij}^{l,k}[N]\geq T_{B,ij}^{l,k}[N]\\ H_B^{l,k}(i,j), & \text{otherwise}\end{cases} \tag{8}$$

Equation (8) illustrates that the final high-frequency coefficient is represented by the coefficient with a larger ignition time (More ignition times). The optimal high-frequency information fusion coefficient is also obtained in the high-frequency part by adaptively adjusting the size of the time decay factor α_e.

In this paper, the new algorithm improves the parameter α_e. The parameter α_e is the time decay constant of $E_{ij}[n]$. Different grayscale images require completely different parameters α_e. In high-intensity regions, a smaller α_e is more suitable for fusing different parts of the image; for darker images, a larger parameter α_e yield better fusion results. In order to select more appropriate parameters α_e, In this paper, we introduce a method to calculate the α_e parameter based on Stevens' power law[19].

$$V=C\times P^n \tag{9}$$

Where, C is constant, V is visual perception intensity, P is actual physical intensity, and index n changes with the change of physical intensity.

When interpreting the relationship between perceived luminance and actual luminance using (9) (the grayscale value of the grayscale image is the actual luminance), Select n=0.5. The target pixels in the general fusion image are mostly high grayscale values, due to the compression of gray scale, a smaller parameter α_e is used to retain more effective image information in order to prevent the dynamic threshold from decaying too fast during the mapping process and thus causing misfires in the neurons corresponding to non-target pixels. Instead, the low grayscale region contains a large number of non-target pixels, so a larger α_e is used to pull up the grayscale in this region to avoid causing information redundancy.

The detailed analysis process is as follows:

(1) The highest grayscale of the background T_{Otsu}. When the difference between the lowest gray level of the target pixel and T_{Otsu} is small or even identical, the smaller α_e is selected to achieve the best fusion results. Otherwise, it is difficult to choose a larger α_e parameter to achieve the desired fusion effect on the image edges. Therefore, the relationship between α_e and T_{Otsu} is set as an inverse relationship in this paper.

(2) The grayscale distribution of the background σ_b. If σ_b is small, it indicates that the grayscale value of the target pixel is almost identical to the overall background pixel, so a smaller α_e is needed for image fusion; If σ_b is larger, a larger α_e will give a better fusion result. On the other hand, σ_b has less effect on the fusion quality when the lowest gray

level of the target pixel is much larger than T_{Otsu}.

In summary, this paper sets α_e and σ_b as a proportional relationship. α_e has a negative relationship with T_{Otsu} and a positive relationship with σ_b. Through extensive experiments, it is found that the algorithm achieves the optimum between fusion quality and computational efficiency when the relationship between the three satisfies (10):

$$\alpha_e = \begin{cases} \left(\dfrac{\sigma_b}{T_{Otsu}}\right)^2, if \dfrac{\sigma_b}{T_{Otsu}} > 0.1 \\ \dfrac{\sigma_b}{T_{Otsu}}, else \end{cases} \tag{10}$$

The above PAPCNN model[15] is mainly applied to image segmentation. Experiments have shown that it can also achieve significant results in dealing with image fusion problems. Especially when the high-frequency coefficients obtained by multi-scale transformation are fused, the visual and objective indexes of the algorithm are greatly improved compared with the traditional algorithm. For high-frequency coefficient fusion of multiscale transform, the absolute value of coefficients represents the activity level information to a certain extent, a larger absolute value of the coefficient indicates, to a certain extent, a higher activity level. The PCNN model is based on pixel intensities for image segmentation. The improved PAPCNN inherits its advantages in image segmentation by fusion of high-frequency parts, and also enhances the ability to adjust the dynamic threshold E, resulting in a more stable activity metric[16]. Therefore, the improved PAPCNN model can extend the image fusion domain from the image segmentation domain, and the above-mentioned improved PAPCNN model is chosen as the fusion scheme for multi-scale transformed high-frequency coefficients.

3.3 Low-frequency sub-band coefficient fusion

After the image is decomposed, part of the important detail information will be retained in the low-frequency part, so the low-frequency part fusion process is also a key part in image fusion. The new algorithm selects latent low-rank to represent the fusion low-frequency coefficients[20]. First, the low-frequency part is decomposed to obtain the significant part L_{C_s} and the low-rank part L_{C_lrr}, where $C \in \{A, B\}$; Then, according to the characteristics of the information contained in the low-rank part and the significant part, the weighted average fusion strategy and the summation fusion strategy are used to get the fused low-rank part L_{lrr} and the significant part L_S; Finally, the fused low-frequency coefficients are obtained by accumulating the low-rank and significant parts. Fig.4 illustrates the low-frequency part of the fusion process.

LatLRR algorithm decomposes the image into two parts: global structure and locally significant structure, which overcomes the problems of inconspicuous saliency features, insufficient protection of primary information, and artifacts after fusion by traditional low-frequency algorithms. In this paper, it is considered effective to use LatLRR algorithm for low-frequency sub-band information fusion. The LatLRR algorithm approximates the low-frequency coefficients both globally and locally, which can fully preserve the significant information of the image, and the experimental results are also more natural. Based on the advantages of LatLRR algorithm, we adopt the LatLRR algorithm model as the fusion scheme of multi-scale transformed low-frequency parts.

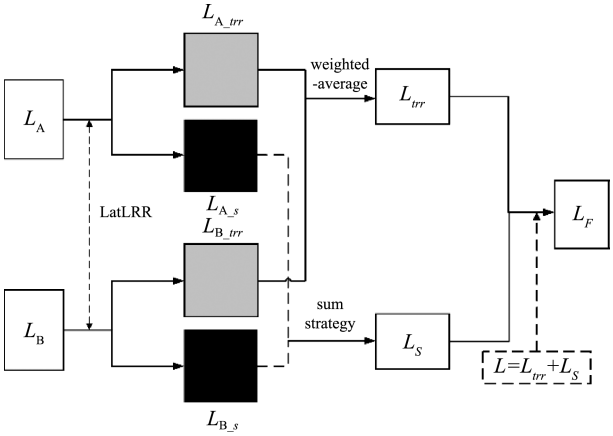

Fig.4. Flow chart of Latent Low-Lank Representation algorithm

3.4 NSST reconstruction

The inverse NSST only requires a non-down sampling shear to sum the coefficients $H_F^{l,k}$ and L_F that have been derived to obtain the final fused image F.

4 Experimental results and analysis

4.1 Image fusion quality evaluation index

In practical applications, visual subjective evaluation of image fusion quality mainly relies on the human visual system for subjective assessment of fused images, which is practical for some specific fusion scenarios. However, it has disadvantages such as strong subjectivity and one-sidedness. The objective evaluation method analyzes the performance of the six fusion methods through objective indicators, and the evaluation results are more instructive.

We have chosen six widely used objective fusion metrics. They are Average Gradient (AG), Space Frequency (SF), Entropy (EN), Mutual Information(MI), Standard Deviation(SD) and edge information retention ($Q^{AB/F}$). SF reflects the rate of change of the image gray scale, and the value of SF is proportional to the similarity between the source image and the experimental result map; AG is the average gradient measure of the image, which is used to measure the clarity of the fused image. EN indicates the information content of the fused image, and higher entropy means better fusion performance; MI measures the degree of similarity between images, and a higher value means that the fused image contains more information from the source image; $Q^{AB/F}$ uses local

metrics to calculate the transfer amount of source image edge information injected into the fusion image; SD reflects the degree of dispersion between pixels. Under normal circumstances, the larger the above six indicators, the better the fusion.

4.2 Methods for comparison

The new algorithm was compared with the traditional PCNN algorithm and five existing representative fusion algorithms, namely, LRR[14], MST-SR[19], NSCT-PCNN[18], NSST-PAPCNN[16] and NSST-PAPCNN-CSR. Among them, MST-SR, NSCT-PCNN, NSST-PAPCNN and NSST-PAPCNN-CSR are all classical fusion schemes based on multi-scale transformation, similar to the fusion framework of the proposed scheme in this paper. LatLRR algorithm fuses the whole image and can be compared with the algorithm in this paper. The parameter values used in these scenarios are the default values provided by the author.

4.3 Image fusion experiments

The images used in this paper are all commonly used fusion images, without any racial or human rights implications. All source images were acquired from the same slice with different imaging methods at the same angle. We selected 80 sets of brain source images for fusion testing to verify the outstanding performance of the algorithm in this paper. Among them, 20 sets each of CT/MR, MR-T1/MR-T2, MR/PET, and MR/SPECT images were used. The selected source images were spatially resolved at 256×256 pixels and were accurately matched before use. In this section, the new algorithm (NSST-PAPCNN-LatLRR) is comprehensively compared with the traditional algorithm PCNN and five mainstream algorithms. It is proved that the algorithm of this paper is leading in both subjective and objective metrics evaluation.

4.3.1 Visual quality

Fig.5 to Fig.8 show the experimental results of the four sets of different modality images. Comparing Fig.c and Fig.i, it can be seen that the fusion effect of the improved PCNN algorithm has a large improvement, and the proposed model is superior to the classical PCNN fusion model. The information of MRI images of MST-SR, NSCT-PCNN, and NSST-PAPCNN (Fig.5e-g) in Fig.5 is over-enhanced, and the overall brightness of the fused images is high; the NSST-PAPCNN-CSR (Fig.5h) algorithm performs convolutional sparse representation of low frequencies as a whole, which leads to blurring of key information in the experimental results; LatLRR and the new algorithm fuse the effective information of CT/MRI images better, where LatLRR fused images lack the protection of details and grain, and the algorithm in this paper overcomes the above shortcomings and has better performance. The LatLRR fusion image in Fig.6 (Fig.d) lacks contrast in overall brightness; the MST-SR, NSCT-PCNN, and NSST-PAPCNN-CSR fusion images (Fig.6e, Fig.6g, Fig.6i) have limited detail extraction ability and lack effective protection of detail information, resulting in a blurred overall visual effect; the NSST-PAPCNN and the new algorithm fusion effect is significantly better than other algorithms, but the algorithm of this paper is significantly better than the NSST-PAPCNN algorithm for processing the grain and edge. In Fig.7, the fused images of MST-SR, NSST-PAPCNN, and NSST-PAPCNN-CSR (Fig.7e, Fig.7g, Fig.7i) have obvious artifacts and low local brightness; LatLRR (Fig.7d) and NSCT-PCNN (Fig.7f) have higher overall visual quality, and the details of the images can be well The texture of the new algorithm (Fig.7i) is clearer and the significant features are more obvious, and there is no noise interference such as artifacts. LatLRR, MST-SR, and NSCT-PCNN (Fig.8d-Fig.8f) fused images in Fig.8 introduced obvious noise, and the overall fusion effect was poor; NSST-PAPCNN-CSR (Fig.8h) retained too much information in the MR source image, resulting in high local brightness; NSST-PAPCNN (Fig.8g) and the new The fused images of NSST-PAPCNN (Fig.8g) and the new algorithm (Fig.8i) fully reflect the key information of the source images, but there are also a small number of artifacts, and the new algorithm has higher clarity of detail information. The NSST-PAPCNN- LatLRR algorithm proposed in this paper (Fig.8g) fully preserves the effective information of the source image, and the low-frequency band also contains part of the detail information. The second decomposition of the low-frequency sub-band information by LatLRR algorithm fully preserves the global structure and significant information structure of the low-frequency segment. Therefore, the detail information contained in the low-frequency segment can be well preserved. The high-frequency sub-band information is fused by the improved PAPCNN model, and the new algorithm obtains the optimal value of this target parameter by the improved parameter αe algorithm, and the fused image can fully retain the significant detail information of the source image without the problem of inappropriate overall brightness of other algorithms, and can also clearly represent the contour, texture and the fused image can fully retain the significant detail information of the source image without the problem of inappropriate overall brightness of other algorithms, and can also clearly represent the contour, texture and edge features of the image without the problem of blurred details or even loss and obvious noise artifact.

4.3.2 Objective evaluation

Table 1 objectively evaluates the performance of different fusion algorithms for medical image fusion. The data of six metrics corresponding to the fused images for the six algorithms are given. For each metric, the highest scores of the six algorithms are shown in bold, and the data ranked second and third are underlined. The top three scores are indicated by their ranking with numbers in parentheses. To more visually compare the objective metrics of different fusion schemes, we visualize the data content in Table 1 as shown in Fig.9.

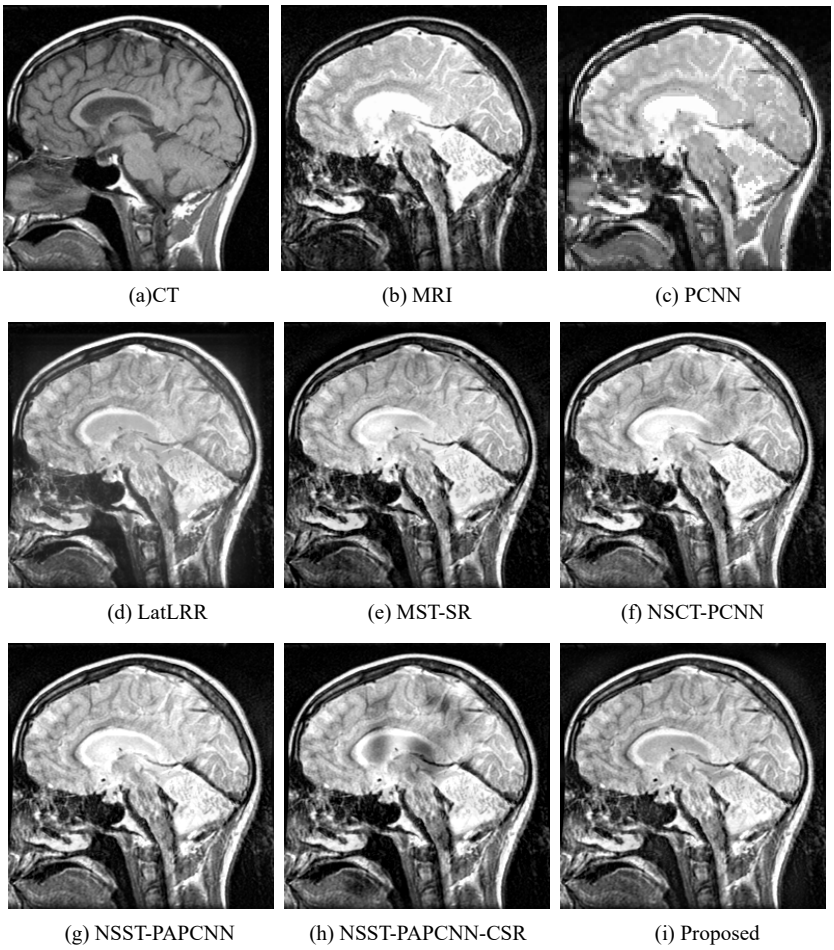

(a)CT (b) MRI (c) PCNN

(d) LatLRR (e) MST-SR (f) NSCT-PCNN

(g) NSST-PAPCNN (h) NSST-PAPCNN-CSR (i) Proposed

Fig.5 CT and MR medical image fusion results.

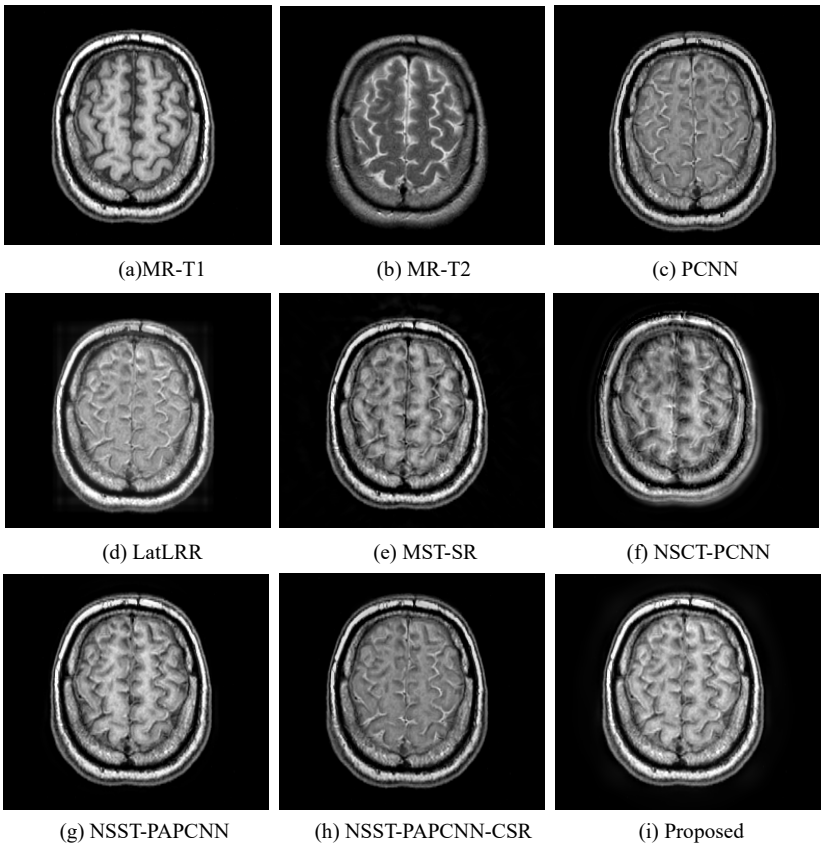

(a)MR-T1 (b) MR-T2 (c) PCNN

(d) LatLRR (e) MST-SR (f) NSCT-PCNN

(g) NSST-PAPCNN (h) NSST-PAPCNN-CSR (i) Proposed

Fig.6 MR-T1 and MR-T2 medical image fusion results.

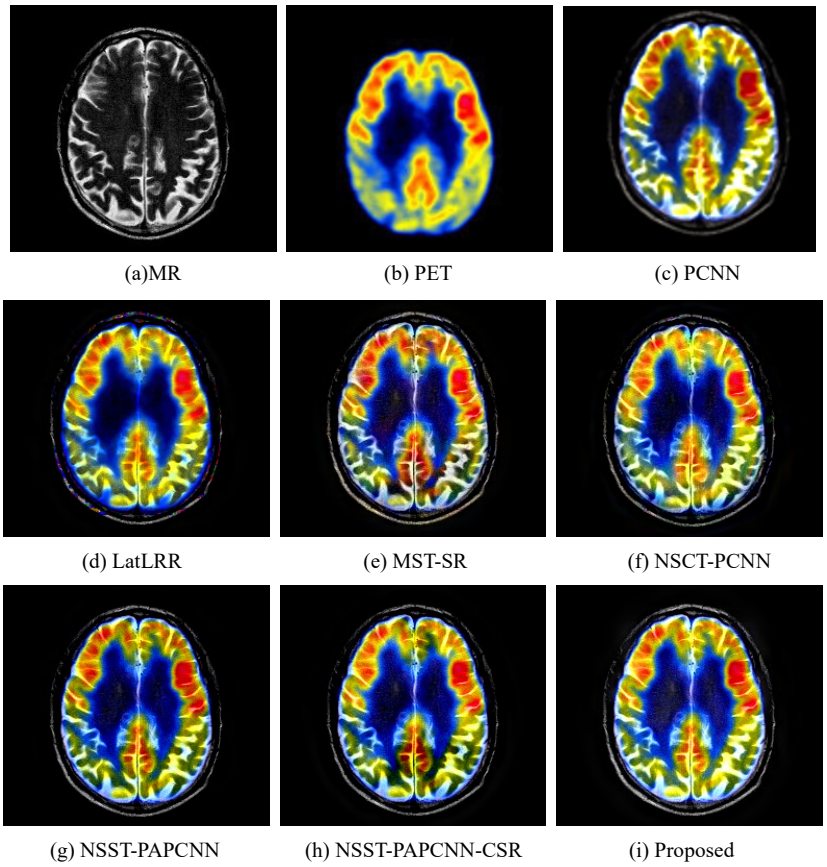

(a)MR (b) PET (c) PCNN

(d) LatLRR (e) MST-SR (f) NSCT-PCNN

(g) NSST-PAPCNN (h) NSST-PAPCNN-CSR (i) Proposed

Fig.7. MR and PET medical image fusion results.

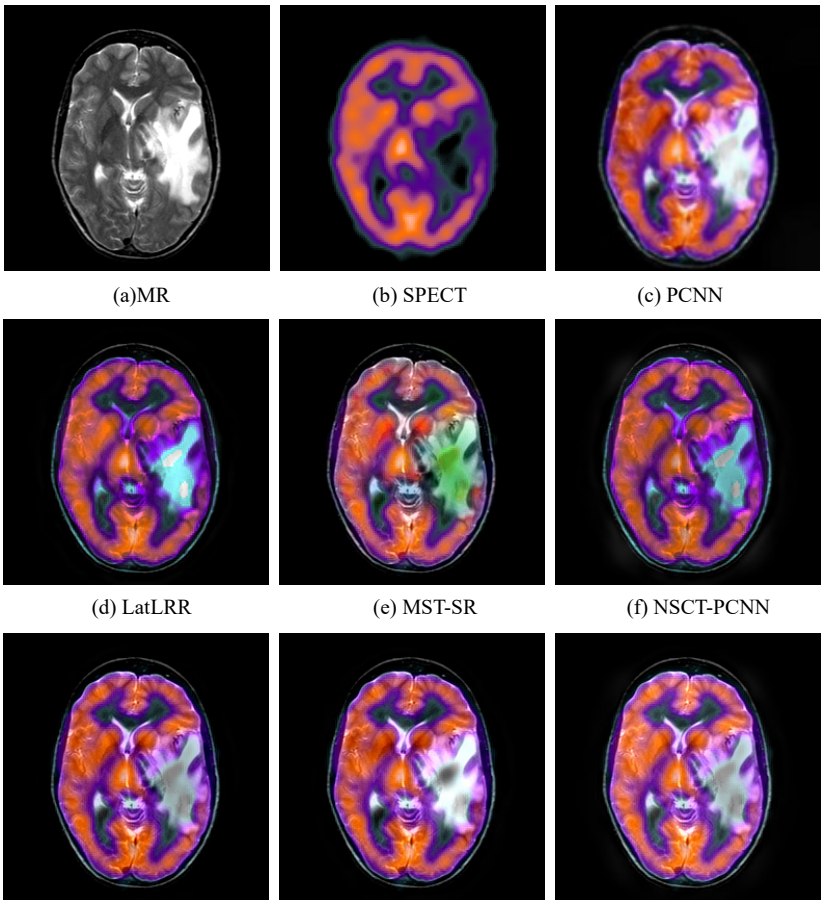

(a)MR (b) SPECT (c) PCNN

(d) LatLRR (e) MST-SR (f) NSCT-PCNN

(g) NSST-PAPCNN (h) NSST-PAPCNN-CSR (i) Proposed

Fig.8 MR and SPECT medical image fusion results.

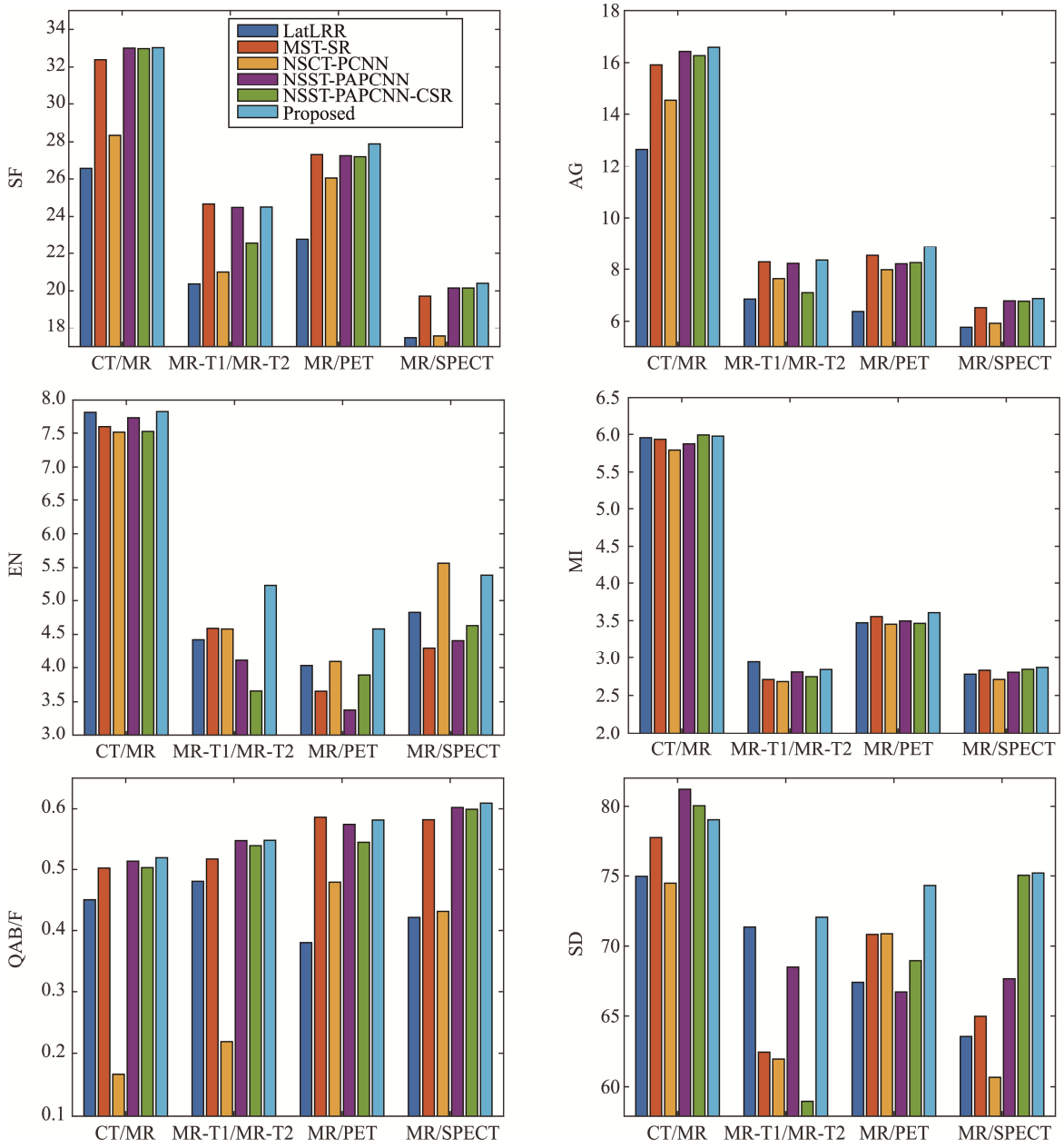

Fig.9 Six image fusion methods for objective evaluation of visual graphics

Table 1 Objective evaluation of different medical image fusion methods

Images	Metrics	LatLRR	MST-SR	NSCT-PCNN	NSST-PAPCNN	NSST-PAPCNN-CSR	Proposed
CT/MR	SF	26.562	32.3869	28.3453	33.0035②	32.978 ③	33.0266 ①
	AG	12.6594	15.9146	14.5297	16.4285②	16.2706 ③	16.5895 ①
	EN	7.8073 ②	7.5956	7.5137	7.7279 ③	7.5252	7.8177 ①
	MI	5.9566 ③	5.9347	5.7921	5.8742	5.9926 ①	5.977 ②
	$Q^{AB/F}$	0.4495	0.5023	0.1653	0.5136 ②	0.503 ③	0.5192 ①
	SD	74.9712	77.7177	74.4846	81.2083 ①	80.0451 ②	78.981 ③
MR-T1/ MR-T2	SF	20.3689	24.668①	20.9992	24.4838 ③	22.5898	24.5038 ②
	AG	6.8512	8.2826②	7.6368	8.2234 ③	7.095	8.3514 ①
	EN	4.4209	4.5898②	4.5801③	4.1088	3.657	5.2241 ①
	MI	2.9431 ①	2.7097	2.6821	2.8093 ③	2.7476	2.8412 ②
	$Q^{AB/F}$	0.4809	0.5171	0.2188	0.5469 ②	0.5387 ③	0.5474 ①
	SD	71.3351②	62.4381	61.8906	68.525 ③	59.0081	72.0205 ①

(Table 1)

Images	Metrics	LatLRR	MST-SR	NSCT-PCNN	NSST-PAPCNN	NSST-PAPCNN-CSR	Proposed
MR/PET	SF	22.7939	27.335②	26.0492	27.275 ③	27.2209	27.8957 ①
	AG	6.3729	8.5347②	7.9795	8.2077	8.2539 ③	8.8776 ①
	EN	4.0299 ③	3.6541	4.0896②	3.3786	3.8903	4.5803 ①
	MI	3.4716	3.5542②	3.4526	3.4967 ③	3.4647	3.6057 ①
	$Q^{AB/F}$	0.3806	0.5849①	0.4975	0.5734 ③	0.5442	0.5804 ②
	SD	67.3905	70.816③	70.864②	66.7107	68.9739	74.3213 ①
MR/SPECT	SF	17.468	19.7207	17.5577	20.1509 ③	20.1522 ②	20.4036 ①
	AG	5.7678	6.5176	5.923	6.7812 ②	6.7689 ③	6.8702 ①
	EN	4.8257 ③	4.2975	5.5651①	4.4068	4.6301	5.3754 ②
	MI	2.7797	2.8309③	2.7102	2.8053	2.8445 ②	2.8684 ①
	$Q^{AB/F}$	0.4211	0.5809	0.4307	0.6023 ②	0.5994 ③	0.6093 ①
	SD	63.5518	64.9827	60.6428	67.6434 ②	75.0464 ③	75.2073 ①

Fig.9 shows. Among the four sets of fused images, the new algorithm is in the top three for all six metric parameters. Among all the six fusion metrics, our scheme is the only one that consistently ranks in the top three for all metrics. Especially for indexes AG, the new algorithm is a substantial improvement, all in the first position. The algorithm in this paper has the same fusion framework as the NSST-PAPCNN and NSST-PAPCNN-CSR algorithms, but the proposed method outperforms both of them in all four sets of fused images, which shows the clear advantage of our method. The MST-SR algorithm obtains high scores in AG metrics for both sets of photos, which is consistent with the advantages of the sparse representation model, but the algorithm in this paper is leading in all other metrics. The above experimental results verify that the new algorithm can achieve greater competitiveness in advanced image fusion schemes.

5 Conclusion

For the shortage of traditional image fusion algorithm, a new fusion algorithm is proposed in this paper. The innovation of this scheme is mainly in two aspects. First, we introduce the PAPCNN model to decompose the fusion of the high-frequency part of the image, and the algorithm of the time decay factor α_e parameter is optimally adjusted better to coordinate the decay rate of the dynamic threshold E. Then, the latent low-rank representation algorithm is introduced into the low-frequency part fusion for the first time to address the problem that the traditional algorithm tends to ignore the effective information in the low-frequency part. It solves the problems of low precision of parameter setting and insufficient protection of detail capability in PCNN model. To verify the fusion performance of the new algorithm, a large number of medical images are selected for experiments and compared with five advanced image fusion schemes. The fusion results show a significant improvement in the visual effects of the new algorithm, and the objective indexes are in the leading position. In our further work, we will develop more efficient image fusion strategies to enhance the protection of valid information and improve the practical applications of image fusion. In addition, we will explore the potential of new algorithms for remote sensing images, infrared and visible images, and other areas.

Author Contributions:

Zirui Tang: Conceptualization; Writing - original draft preparation; Methodology.

Xianchun Zhou: Writing - review and editing; Formal analysis; project administration.

Funding Information:

This research was funded by the National Natural Science Foundation of China, grant number 61302188.

Data Availability:

The authors declare that the main data supporting the findings of this study are available within the paper and its Supplementary Information files.

Conflict of Interest:

The authors declare no competing interests.

Dates:

Received 12 January 2024; Accepted 5 May 2024; Published online 30 June 2024

References

[1] J. Du, W. Li, K. Lu, B. Xiao, “An overview of multi-modal medical image fusion,” Neurocomputing, vol. 215, pp. 3-20, 2016.

[2] B. Jin, Z. Jing, H. Pan. “Multi-modality image fusion via generalized Riesz-wavelet transformation,”KSII Transactions on Internet and Information Systems (TIIS), vol.8(11),pp.

4118-4136. 2014.

[3] R. Singh, A. Khare, “Fusion of multimodal medical images using Daubechies complex wavelet transform—A multiresolution approach,” Information fusion,vol.19, pp. 49-60, 2014.

[4] G. Bhatnagar, Q. M. J. Wu, Z. Liu, “A new contrast based multimodal medical image fusion framework,” Neurocomputing, vol. 157, pp. 143-152, 2015.

[5] Q. Wang, S. Li, H. Qin, A. Hao, “Robust multi-modal medical image fusion via anisotropic heat diffusion guided low-rank structural analysis,” Information fusion, vol. 26, pp. 103-121, 2015.

[6] W.S Ding, D.Y Bi, L.Y He, “Infrared and visible image fusion based on sparse features,” Acta Photonica Sinica, vol. 47(9), pp. 1-10, 2018.

[7] G. Liu, Z Lin, Y. Yu, “Robust subspace segmentation by low-rank representation,” In: The 27th International Conference on Machine Learning, vol.1, pp.8, 2010.

[8] H. Li, X. J. Wu, “Multi-focus Image Fusion Using Dictionary Learning and Low-Rank Representation,” International Conference on Image and Graphics,vol.10666, pp:675-686,2017.

[9] H. Li, X. J. Wu, “Infrared and visible image fusion using Latent Low-Rank Representation,” arxiv preprint arxiv, 1804.08992, 2018.

[10] M. Yin, X. Liu, Y. Liu, “Medical Image Fusion With Parameter-Adaptive Pulse Coupled Neural Network in nonsubsampled shearlet Transform Domain,” IEEE Transactions on Instrumentation and Measurement, vol. 68(1), pp.49-64, 2019.

[11] S. Singh, D. Gupta, R. S. Anand. “Nonsubsampled shearlet based CT and MR medical image fusion using biologically inspired spiking neural network,” Biomedical Signal Processing and Control, vol.18, pp.91-101, 2015.

[12] Z. Guo, Y. Song, Y. Zhao, “An adaptive infrared image segmentation method based on fusion SPCNN,” Signal Processing: Image Communication, vol.87, 115905, 2020.

[13] Xiaojun Z. Image denoising and segmentation model construction based on IWOA-PCNN[J]. Scientific Reports, 2023, 13 (1): 19848-19848.

[14] Xiaomin L, Haowen Y. An Algorithm to Generate a Weighted Network Voronoi Diagram Based on Improved PCNN[J]. Applied Sciences, 2022, 12 (12): 6011-6011.

[15] JingXing L,DaiJun Z,JingXiu Z, et al. Non-negative low-rank representation with similarity correction for cell type identification in scRNA-seq data.[J]. IEEE/ACM transactions on computational biology and bioinformatics, 2023, PP.

[16] Shenghai L, Xuya L, Ruyi H, et al. Image inpainting exploiting global prior refined weighted low-rank representation[J]. Optics and Laser Technology, 2024, 169.

[17] Chiwei G, Ziwei X, Xiuhong C. Multi-view clustering with Laplacian rank constraint based on symmetric and nonnegative low-rank representation[J]. Computer Vision and Image Understanding, 2023, 236.

[18] Minghe L, Zailin Y, Yong Y. Wave effect of front topography based on modified time–frequency transform method[J]. Acta Mechanica, 2023, 234 (7): 3081-3089.